

CONVEX ANALYSIS FOR SEPARATION OF FUNCTIONAL PATTERNS IN DCE-MRI: A LONGITUDINAL STUDY TO ANTIANGIOGENIC THERAPY

Tsung-Han Chan^{1,2}, Li Chen¹, Peter L. Choyke³, Chong-Yung Chi², and Yue Wang¹

¹Dept. of Electrical and Computer Eng., Virginia Polytechnic Institute and State University, Arlington, VA, USA

²Institute of Communications Eng. and Dept. of Electrical Eng., National Tsing Hua University, Hsinchu, Taiwan

³Molecular Imaging Program, National Cancer Institute, National Institutes of Health, Bethesda, MD, USA

ABSTRACT

Dynamic contrast-enhanced magnetic resonance imaging (DCE-MRI) can characterize vascular heterogeneity, and has potential utility in assessment of the efficacy of angiogenesis inhibitors in cancer treatment. Due to the heterogeneous nature of tumor microvasculature, the measured signals can be represented as the mixture of the permeability images corresponding to different perfusion rates. We recently reported a hybrid convex analysis of mixture framework for unmixing of non-negative yet dependent angiogenic permeability distributions (APDs) and perfusion time activity curves (TACs). In our last work, we presented an underlying theory to infer the concept that the TACs can be identified by finding the lateral edges of an observation-constructed convex pyramid when the well-grounded points exist for all APDs. For fulfilling this concept, a hybrid method including non-negative clustered component analysis, convex analysis, and least-squares fitting with non-negativity constraints was developed. In this paper, we use computer simulations to validate the performance of our reported framework, and further apply it to three sets of real DCE-MRI data, before and during the treatment period, for assessing the response to antiangiogenic therapy. The experimental results are not only surprisingly meaningful in biology and clinic, but also capable of reflecting the efficacy of angiogenesis inhibitors in cancer treatment.

Index Terms—Blind source separation, compartment latent variable model, convex analysis, dynamic contrast-enhanced magnetic resonance imaging, antiangiogenic therapy

1. INTRODUCTION

Dynamic functional imaging promises powerful tools for the visualization and elucidation of important disease-causing biological processes in the living tissue. In dynamic contrast-enhanced magnetic resonance imaging (DCE-MRI), recent effort aims to dissect the spatial-temporal patterns of microvascular permeability with differential perfusion rates, where the signal at each pixel often represents a composite

of more than one distinct permeability source independent of spatial resolution [1-3].

Many approaches have been reported for decomposition of the mixtures of biomarkers in dynamic image formation, for example, non-negative independent component analysis (nICA) [4], stochastic non-negative ICA (SNICA) [5], least-correlated component analysis (nLCA) [6], non-negative matrix factorization (NMF) [7] and the NMF-like algorithms with smoothness constraint [8] and with sparseness constraint [9]. The major limitations of these existing algorithms may be the unrealistic assumptions of the compartment model [4], intractable computational complexity [5], and vulnerability to noise contamination [6] and algorithm initialization [7]. To be practically applicable to real DCE-MRI data which may heavily suffered from noise effect and partial volume effect (PVE) [10], we recently proposed a hybrid blind source separation (BSS) approach [11] that utilizes convex analysis, scatter plot clustering and least-squares fitting with non-negativity constraint to recover the non-negative yet correlated angiogenic permeability distributions (APDs) and the associated perfusion time activity curves (TACs). Since DCE-MRI has been suggested as a potential endpoint for assessment of antiangiogenic therapy [12], we applied our reported hybrid framework [11] to three sets of DCE-MRI data before and during antiangiogenic therapy for monitoring the response to therapy. In the longitudinal study, we found that our experimental results are consistent with clinical assessment of a responsive case, surprisingly meaningful in biology and clinic, and indeed able to reflect the efficacy of angiogenesis inhibitors in cancer treatment.

2. PROBLEM FORMULATION

Consider a compartment latent variable model [13] of DCE-MRI as follows:

$$\mathbf{x}(i) = \mathbf{A}\mathbf{k}(i) \quad (1)$$

for $i = 1, \dots, N$, where $\mathbf{x}(i) = [x(i, t_1), x(i, t_2), \dots, x(i, t_L)]^T$ stands for the tracer activities at pixel i measured over L time points, $\mathbf{A} = [\mathbf{a}_f, \mathbf{a}_s, \mathbf{a}_p]$ is an $L \times 3$ mixing matrix whose column vectors are the TACs of fast/slow flow and

plasma input, $\mathbf{k}(i) = [k_f(i), k_s(i), k_p(i)]^T$ is a source vector of APDs at the i th pixel, and N is the number of pixels. Alternatively, the compartment latent variable model (1) can be expressed as

$$\mathbf{x}(i) = \sum_{j \in \{f, s, p\}} k_j(i) \mathbf{a}_j \quad (2)$$

which also means that tracer activities $\mathbf{x}(i)$ is a linear combination of \mathbf{a}_j where $j \in \{f, s, p\}$, weighted by $k_f(i)$, $k_s(i)$, and $k_p(i)$. Figure 1 illustrates the mixing process of the source patterns $\mathbf{k}(i)$.

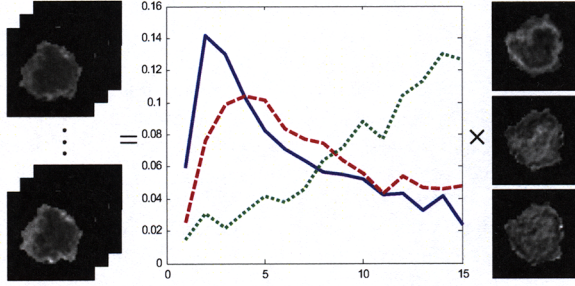


Fig. 1: Compartment latent variable modeling. The 15 observed DCE-MRI images are given in the left column; the supposed ground truth of TACs of plasma input (blue curve), fast flow (red-broken curve) and slow flow (green-dot curve) are shown in the center; the source patterns of interest include the heterogeneous spatial distribution of vascular permeability associated with fast/slow flow (top and middle) and plasma input (bottom) are displayed in the right column.

The goal of recovering APDs $\mathbf{k}(i)$ and TACs \mathbf{A} from the observed tracer activities $\mathbf{x}(i)$ can be formulated as a blind source separation problem, which aims to find a $3 \times L$ unmixing matrix \mathbf{W} from $\mathbf{x}(i)$ such that

$$\hat{\mathbf{k}}(i) = \mathbf{W}\mathbf{x}(i) = \mathbf{W}\mathbf{A}\mathbf{k}(i) = \mathbf{P}\mathbf{k}(i), \quad (3)$$

where $\hat{\mathbf{k}}(i)$ is the estimate of $\mathbf{k}(i)$ up to a permutation \mathbf{P} .

To be practically meaningful in DCE-MRI, we shall make some assumptions for $\mathbf{k}(i)$ and \mathbf{A} as follows:

- (A1) All the elements of $\mathbf{k}(i)$ are non-negative.
- (A2) For each source $j \in \{f, s, p\}$, there exists a pixel index $i_{WGP,j}$ such that $k_j(i_{WGP,j}) > 0$ and $k_l(i_{WGP,j}) = 0$ for all $l \neq j$.
- (A3) The mixing matrix \mathbf{A} is of full column rank.

Assumption (A1) is true in DCE-MRI where the intensities of APDs are represented by non-negative real numbers. Assumption (A2) is made by the observation that in DCE-MRI the vasculatures of different compartments have their own unique perfusion patterns. This kind of pixels in APDs $\mathbf{k}(i_{WGP,j})$, $j \in \{f, s, p\}$ is referred to as *well grounded points (WGPs)*. Figure 2 illustrates the geometric

meaning of the well-grounded points in 3D scatter plot of APDs, where the well-grounded points are located at the axes of the scatter plot. The observed pixels mixed from well-grounded points $\mathbf{k}(i_{WGP,j})$, $j \in \{f, s, p\}$ thus have the same dynamic patterns as \mathbf{a}_j scaled by $k_j(i)$, i.e.,

$$\mathbf{x}(i_{WGP,j}) = k_j(i_{WGP,j}) \mathbf{a}_j, \quad j \in \{f, s, p\}. \quad (4)$$

Assumption (A3) is valid because of the heterogeneous property of vascular permeability, and the number of image acquisition time points L is usually greater than or equal to 3.

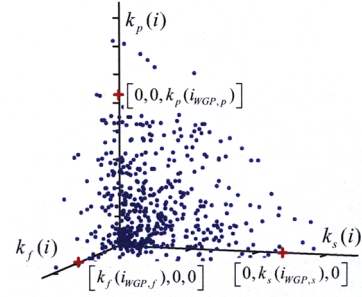


Fig. 2: An illustration of 3D scatter plot of the APDs (blue dots), where the red crosses on each axis are the well-grounded points.

3. THEORY AND METHODS

The purpose of this section is to provide a concise and self-contained description to our reported hybrid convex analysis of mixture framework in [11]. One may refer to [14] to have basic concepts of convex analysis which play an important role in this framework.

3.1 Convex analysis to compartment model

We exploit convex geometry to analyze the compartment latent variable model (1) in which the number of sources, denoted by K , is never limited to 3. Hence, for ease of later use we adopt the following signal model instead of (2):

$$\mathbf{x}(i) = \sum_{j=1}^K k_j(i) \mathbf{a}_j, \quad (5)$$

and also define a set of all the observed tracer activities $X \triangleq \{\mathbf{x}(1), \dots, \mathbf{x}(N)\}$, as well as a set of all the column vectors $A \triangleq \{\mathbf{a}_1, \dots, \mathbf{a}_K\}$. A *convex pyramid* of A is the set of all the non-negative combinations of $\mathbf{a}_1, \dots, \mathbf{a}_K$, defined as

$$\mathbb{P}_{\text{convex}} \{A\} = \left\{ \sum_{j=1}^K \alpha_j \mathbf{a}_j \mid \mathbf{a}_j \in A, \alpha_j \geq 0 \right\}.$$

in which the vectors $\mathbf{a}_1, \dots, \mathbf{a}_K$ are called *lateral edges* of $\mathbb{P}_{\text{convex}} \{A\}$ when $\mathbf{a}_1, \dots, \mathbf{a}_K$ are linearly independent.

Any observed pixel $\mathbf{x}(i) \in X$ can always be represented as (5), and under (A1) and (A3) it is easy to show $\mathbf{x}(i) \in \mathbb{P}_{\text{convex}} \{A\}$, so we can infer that $X \in \mathbb{P}_{\text{convex}} \{A\}$

whose lateral edges are given by $\mathbf{a}_1, \dots, \mathbf{a}_K$. This implies that all the observed pixels $\mathbf{x}(i)$ are enclosed by a convex pyramid of A . With the existence of WGs [(A2)], we shall be possible to obtain the information about $\mathbf{a}_1, \dots, \mathbf{a}_K$ from the set X , as described in the following theorem.

Theorem 1. (Identifiability [10]) Under (A1), (A2) and (A3), the lateral edges of $\mathbb{P}_{\text{convex}}\{X\}$ are $\mathbf{a}_1, \dots, \mathbf{a}_K$.

Theorem 1 suggests a possibility of identifying the mixing matrix \mathbf{A} by finding the lateral edges of $\mathbb{P}_{\text{convex}}\{X\}$. A geometric illustration of Theorem 1 for $K=3$ is shown in Fig. 3. The blue dots are the observed pixels $\mathbf{x}(1), \dots, \mathbf{x}(N)$ forming the convex pyramid $\mathbb{P}_{\text{convex}}\{X\}$, and the red arrows are the three lateral edges of $\mathbb{P}_{\text{convex}}\{X\}$ which are able to enclose all the observed pixels.

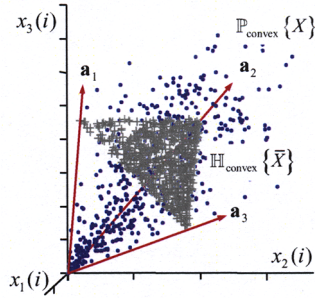


Fig. 3: An illustration of 3D scatter plot of observed pixels.

By performing a normalization procedure to the observed pixels $\mathbf{x}(1), \dots, \mathbf{x}(N)$ in the following manner

$$\bar{\mathbf{x}}(i) = \frac{\mathbf{x}(i)}{\mathbf{1}^T \mathbf{x}(i)} = \sum_{j=1}^K \left(\frac{k_j(i) \mathbf{1}^T \mathbf{a}_j}{\mathbf{1}^T \mathbf{x}(i)} \right) \left(\frac{\mathbf{a}_j}{\mathbf{1}^T \mathbf{a}_j} \right) = \sum_{j=1}^K \bar{k}_j(i) \bar{\mathbf{a}}_j, \quad (6)$$

where $\bar{k}_j(i) = k_j(i) \mathbf{1}^T \mathbf{a}_j / \mathbf{1}^T \mathbf{x}(i)$ and $\bar{\mathbf{a}}_j = \mathbf{a}_j / \mathbf{1}^T \mathbf{a}_j$ such that $\sum_{j=1}^K \bar{k}_j(i) = 1$ and $\mathbf{1}^T \bar{\mathbf{a}}_j = 1$, we can show that the problem for identifying the lateral edges of a convex pyramid suggested by Theorem 1 is then converted into the search of the extreme points of a convex hull of the normalized observed pixels $\bar{X} \triangleq \{\bar{\mathbf{x}}(1), \dots, \bar{\mathbf{x}}(N)\}$, say

$$\mathbb{H}_{\text{convex}}\{\bar{X}\} = \left\{ \sum_{i=1}^L \alpha_i \bar{\mathbf{x}}(i) \mid \bar{\mathbf{x}}(i) \in X, \alpha_j \geq 0, \sum_{i=1}^L \alpha_i = 1 \right\},$$

as stated in the following lemma.

Lemma 1 (Normalization [11]). Under (A1), (A2) and (A3), the convex pyramid $\mathbb{P}_{\text{convex}}\{X\}$ becomes a convex hull

$\mathbb{H}_{\text{convex}}\{\bar{X}\}$ whose extreme points are the normalized lateral edges (or $\bar{\mathbf{a}}_1, \dots, \bar{\mathbf{a}}_K$).

A geometric illustration of Lemma 1 is shown in Fig. 3. The gray crosses are the normalized observed pixels which form a triangle in 3D scatter plot space. The region of the triangle is exactly the convex hull of the normalized lateral edges $\bar{\mathbf{a}}_1, \dots, \bar{\mathbf{a}}_K$. Such problem to search for the extreme points of a convex hull is called an extreme point enumeration problem in optimization context, and can be solved by quickhull algorithm [15].

3.2 Methods

Let us turn our attention back to DCE-MRI applications where $K=3$. The real data may be heavily affected by noise and partial volume effect (PVE) [10] which are not considered in our theoretical derivations, thus exploring its application to DCE-MRI in practice is the subject of ensuing developments.

3.2.1 Non-negative clustered component analysis

The non-negative clustered component analysis (nCCA) [16] is designed to remove noise effect in this framework, assuming the following Gaussian mixture model for pure-volume pixels

$$\mathbf{x}_n(i) = \mathbf{a}_j + \boldsymbol{\varepsilon}(i), \quad j \in \{f, s, p\}, \quad (7)$$

where $\mathbf{x}_n(i)$ is the noisy observed pixel and $\boldsymbol{\varepsilon}(i)$ is a zero-mean Gaussian noise vector. The EM algorithm is employed to cluster the normalized noisy observed pixels $\bar{\mathbf{x}}_n(i)$ for noise removal. For instance, the resulting cluster centers $\bar{\mathbf{x}}_c(i)$ for $i=1, \dots, P$ are thought of as the noise-removed observed pixels, where P is the pre-assigned number of Gaussian kernels to be clustered.

3.2.2 Convexity measure

Although nCCA can be pre-applied for noise removal, selecting 3 extreme points capable of enclosing all the noise-removed observed pixels is still unrealistic due to PVE. Here we reported a *convexity measure* (CM) [11] to choose 3 cluster centers in $X_c \triangleq \{\bar{\mathbf{x}}_c(1), \dots, \bar{\mathbf{x}}_c(P)\}$ which can construct a convex hull such that the margin between the convex hull and other cluster centers outside it is minimized. Mathematically, the CM is an optimization problem as follows,

$$CM = \min_{l_1, l_2, l_3} \sum_{i=1}^P e_i(l_1, l_2, l_3), \quad (8)$$

where $\{l_1, l_2, l_3\} \subset \{1, \dots, P\}$, $l_i \neq l_j$ for $i \neq j$ are the indices of the selected cluster centers, and the margin between the i th cluster center $\bar{\mathbf{x}}_c(i)$ and the convex hull can be obtained by

$$e_i(l_1, l_2, l_3) = \min_{\hat{\theta}_1, \hat{\theta}_2, \hat{\theta}_3} \left\| \bar{\mathbf{x}}_c(i) - \sum_{j=1}^3 \hat{\theta}_j \bar{\mathbf{x}}_c(l_j) \right\|_2^2, \quad (9)$$

subject to $\sum_{j=1}^3 \hat{\theta}_j = 1, \hat{\theta}_j \geq 0 \forall j = 1, 2, 3$. The problem (9) is a convex optimization problem and the problem (8) could be solved by an exhaustive search of C_3^P combinatorial possibilities, where P is not very large and usually less than 30.

Suppose that the three clustered centers with minimum CM are estimated, say $\hat{\mathbf{a}}_f, \hat{\mathbf{a}}_s, \hat{\mathbf{a}}_p$, we then can estimate APDs $\mathbf{k}(i)$ by the least-squares fitting under non-negative constraint of $\mathbf{k}(i)$, i.e.,

$$\mathbf{k}(i) = \arg \min_{\mathbf{k}(i)} \left(\left\| \mathbf{x}(i) - \hat{\mathbf{A}} \mathbf{k}(i) \right\|_2 \right) \quad (10)$$

s.t. $k_j(i) \geq 0$ for $j \in \{f, s, p\}$

where $\hat{\mathbf{A}} = [\hat{\mathbf{a}}_f, \hat{\mathbf{a}}_s, \hat{\mathbf{a}}_p]$ is the estimated mixing matrix.

In real DCE-MRI applications, some preprocessing such as region of interest (ROI) extraction and pixel filtering are also essential to making the outcome more successful and meaningful before directly applying unmixing methods to real data set. We summarize the processing steps of our framework as follows:

Given DCE-MRI data X and the number of TACs, $K=3$.

Step 1. ROI extraction. The surrounding normal tissues including the external/internal dark area (i.e., completely dead tissue) are totally removed.

Step 2. Removal of first few DCE-MRI time segments before the agent uptake actually takes place. It shall be very careful since the important information may also be lost here.

Step 3. Observed pixel filtering with hybrid criteria: (a) very low average signal intensity or (b) very low signal variation even with high average signal intensity. Due to physical nature of the signals derived from compartment model, there shall not be any impulse or flat type TACs, while plasma input TAC will be most short-lasting. Note that this step also helps reduce the error of tumor ROI masking in some cases such as internal dark areas.

Step 4. Normalization of the observed pixels in the manner of (6), yielding the set of the normalized observed pixels \bar{X} .

Step 5. Initialization of nCCA by visual aid and human-computer interaction. In medical research, most of people do not consider "automatic" as important as "informative", thus, this step is helpful and potentially effective.

Step 6. Apply nCCA to the data set \bar{X} to obtain P noise-removed observed pixels (clustered centers).

Step 7. Solve convexity measure problem of the P noise-removed observed pixels to estimate three TACs $\hat{\mathbf{a}}_f, \hat{\mathbf{a}}_s, \hat{\mathbf{a}}_p$.

Step 8. Estimate APDs $\mathbf{k}(i)$ by solving the non-negative least-squares problem given by (10).

4. COMPUTER SIMULATIONS

We present some simulation results of our framework for examining the separation capability of the reported framework [11] and compare the performance with two existing unmixing algorithms, nICA [4] and NMF [7] in this section. The simulated data, fifteen DCE-MRI images, were generated by mixing the given 3 TACs and the APDs as shown in Fig. 1. We also added zero mean Gaussian noise to the 15 generated DCE-MRI images such that signal-to-noise ratio (SNR) equals 25 dB, where SNR is defined as $\text{SNR} = \sum_{i=1}^N \|\mathbf{x}(i)\|^2 / \sigma^2 LN$ in which σ^2 is the noise variance. To numerically measure the performance of the various unmixing algorithms, we use the correlation coefficient between TACs and their estimates, given by

$$\rho = \frac{1}{K} \max_{\pi \in \Pi_K} \sum_{i=1}^K \frac{[\mathbf{a}_i - \mathbf{m}(\mathbf{a}_i)]^T [\hat{\mathbf{a}}_{\pi_i} - \mathbf{m}(\hat{\mathbf{a}}_{\pi_i})]}{\|\mathbf{a}_i - \mathbf{m}(\mathbf{a}_i)\| \|\hat{\mathbf{a}}_{\pi_i} - \mathbf{m}(\hat{\mathbf{a}}_{\pi_i})\|}$$

where $\mathbf{m}(\mathbf{a}_i) = (\mathbf{1}^T \mathbf{a}_i / L) \mathbf{1}$ is the mean vector of TAC \mathbf{a}_i ,

and $\Pi_K = \{\pi = (\pi_1, \dots, \pi_N) \mid \pi_i \in \{1, \dots, K\}, \pi_i \neq \pi_j \forall i \neq j\}$

is the set of all permutations $\{1, \dots, K\}$. The larger the value of ρ , the better the performance of the algorithm under evaluation.

The simulation results are given in Table I. The estimated TACs are shown in Fig. 4. Both of Table I and Fig. 4 show that the framework is promising due to much better estimation accuracy for the obtained estimates of TACs and APDs, compared with NMF and nICA.

Methods		Framework	NMF	nICA
ρ	TACs	0.9194	0.8743	0.7835
	APDs	0.7718	0.6636	0.5777

Table I: Performance comparison of ρ over our reported framework, NMF, and nICA.

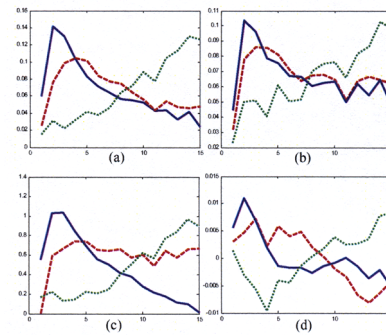


Fig. 4: (a) The true APDs and the estimated APDs obtained by (b) our reported framework, (c) NMF, and (d) nICA. The blue solid, red-broken, and green-dot curves stand for the TACs associated with plasma input, fast flow, and slow flow, respectively.

5. EXPERIMENTS AND DISCUSSION

We report herein the application of our convex analysis of mixtures framework [11] in a longitudinal study to monitor a breast tumor's response to anti-angiogenic therapy. DCE-MRI has been suggested as a potential endpoint in assessment of the response to therapy [12]. Three sets of DCE-MRI data were acquired before and during the treatment period, each with three-months apart. Figure 5 shows three sets of DCE-MRI images and the highlighted regions presenting the same tumor's functional appearance. We can apparently observe that the tumor sizes vary over a half year of longitudinal study, and thus the spatial permeability maps (the APDs or sources) must change for sure. However, we do not know whether the TACs shall change over the treatment period or not. Hence, we consider two hypotheses as follows: in a longitudinal study, (H1) both of TACs and APDs change, and (H2) TACs remain the same but APDs change.

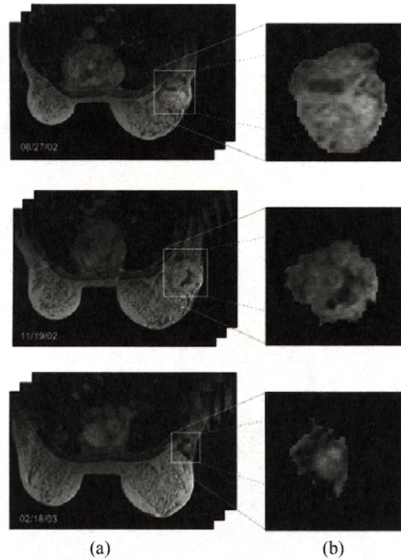


Fig. 5: Three sets of DCE-MRI data of the same tumor were acquired and shown in (a). The tumor sites were depicted via human-computer interaction and are highlighted in (b). The date in the left-bottom area of each data set denotes the acquisition date.

To verify the above two proposed hypotheses, we design two experiments as follows. For hypothesis (H1), we shall apply our reported framework to each of DCE-MRI data sets separately. In the processing steps of the framework, the resultant percentage of the discarded pixels through observed pixel filtering for each data set is listed in Table II, and the pre-assigned number of clusters using in nCCA, say P , is set to 15. The experimental results are shown in Fig. 6. Before treatment starts, most pixels exhibit fast perfusion

and very few pixels of slow perfusion remained; see the top row of Fig. 6. Upon administration of angiogenic inhibitor, a transient “tumor vasculature normalization” takes place [17]. Explicitly, in the beginning of anti-angiogenic therapy, the phenomenon “vessel normalization” occurs in many pixels where the perfusion is significantly reduced; see the middle row of Fig. 6. After treatment, the perfusion in most area is further normalized with slower perfusion, and the original normal microvasculature remains stable as expected; see the bottom row of Fig. 6. The corresponding 3D scatter plot of these three sets of estimated APDs are shown in Fig. 7. Most of the estimated APD pixels are either in the vicinity of the axes or near the coordinate planes of the first quadrant, indicating that all the observed pixels are totally unimixed and bounded by non-negativity.

Data sets	08/27/02	11/19/02	02/18/03
%	16.25	10.24	22.13

Table II: The percentage of the discarded observed pixels for each data set via pixel filtering with hybrid criterion.

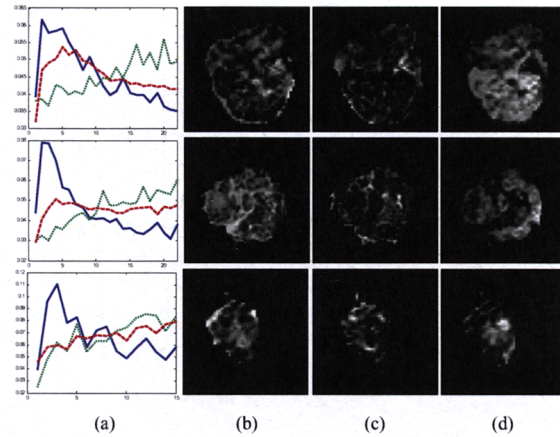


Fig. 6: Three sets of TACs and APDs estimated respectively by our framework in a longitudinal study. (a) The estimated TACs corresponding to fast/slow perfusions and plasma input, and the estimated APDs associated with (b) fast flow, (c) slow flow, and (d) plasma input.

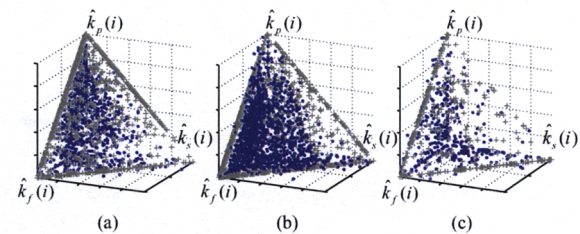


Fig. 7: The 3D scatter plots of the APDs estimated separately via our framework for (a) the data set before treatment, (b) during treatment, and (c) after treatment. The blue dots are the estimated APDs and gray crosses are the normalized APDs.

For hypothesis (H2), we may consider the estimated TAC before the therapy starts as a baseline, and then subsequently estimate the APDs in the follow-up studies to see whether the spatial distribution of fast/slow permeability and plasma input changes. We would expect that the permeability map associated with fast flow shall take less fraction of the total tumor volume during and after the antiangiogenic therapy. The 3D scatter plots of the estimated APDs are shown in Fig. 8. The similar observation as Fig. 7 can be seen that all the observed pixels are unmixed to axes or the coordinate planes of the first quadrant.

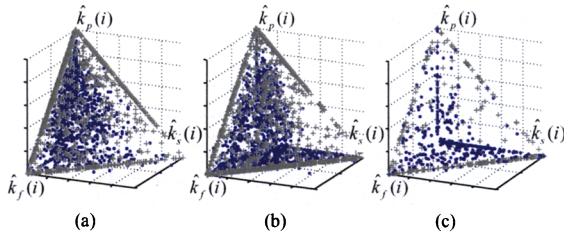


Fig. 8: The 3D scatter plots of the APDs estimated by non-negative least-squares fitting using the estimated TAC before therapy as a baseline. (a) The data set before treatment, (b) during treatment, and (c) after treatment.

Although the case in the longitudinal study does not display a clear active angiogenesis peripheral ring and a hypoxia core which usually appear in spatial permeability maps associated with fast/slow flows, it indicates a more homogeneous spatial mixture or we can say it is a relatively early-stage and very active angiogenic tumor. On the other hand, our results also show that the abnormal structure and function of tumor vasculature are normalized via the administration of anti-angiogenic agents. This observation is surprisingly consistent with the concept reported in [17].

6. CONCLUSION

We have applied our reported hybrid convex analysis of mixture framework [11] to a longitudinal study in DCE-MRI. Our preliminary experimental results coincide with underlying biomedical expectations and this longitudinal study indicated a promising and successful utility of the reported framework for assessing the efficacy of the anti-angiogenic therapy. Given the difficulty of the task, while the optimality of this method may be data-dependent, we would expect it to be a very effective tool in efficacy analysis of angiogenesis inhibitors in cancer treatment.

7. REFERENCES

- [1] D. M. McDonald and P. L. Choyke, "Imaging of angiogenesis: From microscope to clinic," *Nature Medicine*, vol. 9, pp. 713-725, 2003.
- [2] A. R. Padhani and J. E. Husband, "Dynamic contrast-enhanced MRI studies in oncology with an emphasis on quantification, validation and human studies," *Clin. Radiol.*, vol. 56, pp. 607-620, 2001.
- [3] Y. Wang, J. Xuan, R. Srikanthana, and P. L. Choyke, "Modeling and reconstruction of mixed functional and molecular patterns," *International Journal of Biomedical Imaging*, vol. 2006, pp. 1-9, 2006.
- [4] M. D. Plumbley, "Algorithms for non-negative independent component analysis," *IEEE Trans. Neural Netw.*, vol. 14, no. 3, pp. 534-543, 2003.
- [5] S. A. Astakhov, H. Stogbauer, A. Kraskov, and P. Grassberger, "Monte Carlo algorithm for least dependent non-negative mixture decomposition," *Analytical Chemistry*, vol. 78, pp. 1620-1627, 2006.
- [6] F.-Y. Wang, Y. Wang, T.-H. Chan, and C.-Y. Chi, "Blind separation of multichannel biomedical image patterns by non-negative least-correlated component analysis," *Lecture Notes Bioinfo.*, vol. 4146, pp. 151-162, 2006.
- [7] D. D. Lee and H. S. Seung, "Learning the parts of objects by non-negative matrix factorization," *Nature*, vol. 401, no. 6755, pp. 788-791, 1999.
- [8] A. P.-Montano, J. M. Carazo, K. Kochi, D. Lehmann and R. D. P.-Marqui, "Nonsmooth nonnegative matrix factorization," *IEEE Trans. Pattern Analysis and Machine Intelligence*, vol. 28, no. 3, pp. 403-415, Mar. 2006.
- [9] K. Stadlthanner, F. J. Theis, E. W. Lang, A. M. Tome, C. G. Puntonet, J. M. Gorriz, "Hybridizing sparse component analysis with genetic algorithms for microarray analysis," to appear in *Neurocomputing*.
- [10] P. Santago and H. D. Gage, "Statistical models of partial volume effect," *IEEE Trans. Image Processing*, vol. 4, pp. 1531-1540, Nov. 1995.
- [11] L. Chen, T.-H. Chan, P. L. Choyke, C.-Y. Chi, G. Wang and Y. Wang, "Convex analysis and separation of composite signals in DCE-MRI," *IEEE International Symposium on Biomedical Imaging*, Paris, France, May 14-17, 2008.
- [12] A. R. Padhani, "MRI for assessing antivasular cancer treatments," *The British Journal of Radiology*, vol. 76, pp. S60-S80, 2003.
- [13] Y. Zhou, et al., "A modeling-based factor extraction for determining spatial heterogeneity of Ga-68 EDTA kinetics in brain tumors," *IEEE Trans. Nucl. Sci.*, vol. 44, pp. 2522-2527, 1997.
- [14] S. Boyd and L. Vandenberghe, *Convex Optimization*. Cambridge Univ. Press, 2004.
- [15] C. B. Barber, D. P. Dobkin, and H. T. Huhdanpaa, "The quickhull algorithm for convex hulls," *ACM Trans. Mathematical Software*, vol. 22, no. 4, Dec. 1996, pp. 469-483.
- [16] L. Chen, Y. Wang, C.-Y. Chi, Z. Szabo and P. L. Choyke, "Separating composite signals in multi-probe dynamic imaging", *Proc. 41st Annual Asilomar Conference on Signals, Systems, and Computers*, Pacific Grove, CA, Nov. 4-7, 2007, pp. 9-12.
- [17] R. K. Jain, "Normalization of tumor vasculature: An emerging concept in antiangiogenic therapy," *Science*, vol. 307, pp. 58-62, Jan. 7, 2005.